A fast methodology for the accurate characterization and simulation of laser heat treated blanks

A fast methodology for the accurate characterization and simulation of laser heat treated blanks

Attilio Lattanzi[a], Antonio Piccininni[b,*], Pasquale Guglielmi[b], Marco Rossi[a], Gianfranco Palumbo[b]

[a] *Department of Industrial Engineering and Mathematics, Università Politecnica delle Marche, via Brecce Bianche, Ancona, 60131, Italy*
[b] *Department of Mechanics, Mathematics and Management Engineering, Politecnico di Bari, via Orabona 4, Bari, 70125, Italy*

Abstract

In this work, a new methodology for the material characterization of locally heat treated blanks is proposed. Laser treatments on the central part of dog-bone specimens, extracted from a strain hardenable Aluminium sheet (AA5754) in wrought condition (H32), were simulated through an inversely tuned Finite Element model (FE) and performed using a CO_2 laser. In order to establish a correlation between the temperature history in each point and the corresponding material properties after the heat treatment, preliminary local annealing tests were conducted by means of the Gleeble 3180 system; such heat treated samples were then subjected to Vickers microhardness tests along the longitudinal direction in order to obtain data for defining a simple but effective annealing function based on the maximum temperature (T_{peak}) experienced by the material. Tensile tests on the laser

*Corresponding author
Email addresses: a.lattanzi@staff.univpm.it (Attilio Lattanzi), antonio.piccininni@poliba.it (Antonio Piccininni), pasquale.guglielmi@poliba.it (Pasquale Guglielmi), m.rossi@staff.univpm.it (Marco Rossi), gianfranco.palumbo@poliba.it (Gianfranco Palumbo)

heat-treated specimens were assisted by a Digital Image Correlation (DIC) system, which allowed to obtain the full-field deformation history and, as a consequence, to extract different flow stress curves , since each region of the sample was subjected to different temperature levels. The material behaviour in terms of stress vs. strain curves extracted by DIC could be related to the same variable (T_{peak}) and finally implemented into a FE model. The proposed methodology revealed to be effective in extracting the flow stress curves (yielding plus hardening) and, as demonstrated by the simulation of the tensile test, it allowed to predict the deformation behaviour of the material with graded properties more accurately than the qualitative approach based on the assignment of different mechanical properties by partitions.
Keywords: Local properties, Gleeble test, Numerical simulation, Digital Image Correlation, Inverse method

1. Introduction

Over the last years, the increasing costs for energy and raw materials combined with the need of respecting the stricter and stricter CO_2-emissions' limits, are pushing the attention of the vehicle manufacturers to search for robust and effective solutions: the improvement of the propulsion system, despite effective, can only have a secondary impact on reducing polluting emissions [1], whereas its combination with the lightweighting of the structural components has been indicated as the most promising solution to tackle the problem [2, 3] without excessively affecting the vehicle's performance and the passengers' safety [4–6].

The successful implementation of the lightweighting design criteria mainly

depends on the availability of suitable materials and manufacturing processes [7]. In this context, the modern automotive industry often adopts a multi-material approach for the design of complex structures like cars; for instance, aluminium (Al) alloys and the new generation of advanced high strength steels (AHSS) have been successfully employed in BIW structures and chassis in order to reduce the vehicle weight without compromising the safeness [8, 9]. In particular, aluminium alloys are nowadays widely recognized as the ideal candidate since they optimally combine high strength and limited density (if compared with mild steel stamping grades [10–12]). But, even considering their poor formability at room temperature, which limits the widespread application of the Al alloys [13], manufacturing processes surely play a key role.

For this reason, the scientific research has put lots of efforts to remarkably improve the capabilit y of sheet forming technologies to obtain sound complex-shaped components in a very limited number of processing steps [14]. Well assessed methodologies which can be found in literature are: (i) to increase the working temperature, thus switching the forming operation to warm conditions [15–18]; (ii) to use processes able to better exploit the material formability, like, for example, the Single Point Incremental Forming [19] or the Hydroforming [20]; (iii) to locally change the material properties [21, 22] or any characteristic (as, for instance, the thickness [23]) in order to create more favorable forming conditions; (iv) to properly combine the above mentioned ones [24–26].

The approach of locally changing the material properties is considered particularly attractive because the forming operation can be carried out

avoiding complex and expensive tools [22]. Such an innovative approach can be applied by splitting the manufacturing process into two different sub-steps: the blank is locally heated via short-term treatments to obtain an optimal distribution of strength/ductility (according to the component to be manufactured) and subsequently stamped at room temperature. It was successfully used, for example, in the deep drawing of an age-hardenable Al alloy: a remarkable improvement of the limit drawing ratio (LDR) could be achieved by fully solutioning the outer region of the circular specimen while keeping the initial strength in the remaining part [21]. Promising results have been achieved also in the manufacturing of large components as in the case of a tailgate for automotive applications: the local modification of the material properties was obtained via conductive heating (due to the large portion of the blank to be treated) and, together with an optimal blank profile , allowed to improve the material drawability, thus leading to the manufacturing of a sound component [27]. Moreover, the technology is highly flexible since it is applicable not only to the Al alloys but also to different steel stamping grades in wrought conditions [28].

For the implementation of such a methodology, the design of both the sub-steps plays a crucial role: the most robust way to accomplish this task is to adopt accurate Finite Element (FE) models able to properly simulate the forming process. The above mentioned accurateness can be obtained through the effective modelling of the material behaviour that, in turn, relies on the adoption of fast and robust methodologies for both the characterization and the tuning. Many experimental methods are available to identify the constitutive properties of materials; however, an increasing interest has

been dedicated to the inverse methods in recent years. Inverse methods allow to employ data from any kind of test (even non-standard tests), involving, for example, complex and heterogeneous strain – and, consequently, stress – or temperature histories, in order to enrich the material information which can be extracted from a single test [29–31]. Inverse methods can be used in a wide range of applications, often in combination with full-field strain measurements [24, 32] in order to evaluate the spatial deformation of the specimen during the test. Among the different full-field optical techniques, the Digital Image Correlation (DIC) [33, 34] represents by far the most widespread one because of its ease of use, flexibility and availability of dedicated software.

Different types of inverse methods have been used for the material characterization ; one of the most popular methods is the Finite Element Model Updating (FEMU), which is based on the iterative modification of the FE simulation of the experiment in order to identify the optimal parameters of the constitutive model [35]. FEMU has been often applied in plasticity through the adoption of a complex test set-up [36] or specimen's geometries [37]. Besides FEMU, inverse methods that do not rely on FE exist, which directly exploit the full-field measurements to calibrate the constitutive model: for instance, in the Virtual Fields Method (VFM) [38], the equilibrium equation is applied to the experimental strain maps with no need of numerical models. VFM has been extensively used in plasticity, for example to evaluate the anisotropic behaviour [39, 40]. Recently, a sensitivity-based approach was proposed for the non-linear VFM [41, 42] and successfully used to calibrate advanced constitutive models characterised by a large number of parameters to be simultaneously identified [43].

Inverse methods coupled with DIC have been often used to identify the post-necking behaviour of metals [44, 45] and the heterogeneous properties of metals subjected to technological process, e.g. welding [46] or friction stir welding [47, 48]. For this reason a similar approach is assumed to be valid for identifying the hardening behaviour of materials characterised by local mechanical properties , being the alteration due to the different temperature profiles experienced by the material during, for example, a laser treatment.

In the present work, an innovative methodology has been proposed to rapidly characterize the behaviour of an Al alloy in wrought condition (AA5754-H32) locally annealed by laser. As preliminary step, annealing test s were carried out by means of a Gleeble system ; in order to establish a correlation between the local temperature history and the material properties, the treated samples were then subjected to Vickers microhardness tests along the longitudinal direction . A simple but effective annealing function based on the maximum temperature (T_{peak}) locally experienced by the material could be thus defined. According to the preliminary results, laser treatments were simulated via an inversely tuned FE model and performed using a CO_2 laser. Since the laser heating was localized in the central area of the specimen, a temperature gradient was obtained during the treatment which resulted, in turn, in a gradient of properties moving from the treated area, across the heat affected zone, up to the base material. Tensile tests on the locally heat treated specimens were assisted by a DIC measurement system; the deformation field over the whole gauge area could be thus calculated and several flow curves, strictly related to temperature level which was locally experienced by the material, could be extracted from a unique test. The

material behaviour in terms of stress vs. strain curves extracted by DIC could be related to the same variable (T_{peak}) and finally implemented , for validation purposes, into a Finite Element model with the aim of accurately reproducing the tensile test on the leaser heat treated sample.

2. Material and Methods

2.1. The investigated alloy

The Al alloy AA5754 was used for the experiments. It is a strain hardenable Al alloy received in the wrought condition H32. The dogbone specimens (1.5 mm thick) were extracted along the 0° direction (with respect to the rolling one, RD). The chemical composition of the alloy is reported in Table 1.

Table 1: Chemical composition of the investigated alloy (AA5754-H32).

Si	Fe	Cu	Mn	Mg	Cr	Zn	Ti	Al
0.259	0.377	0.067	0.187	3.057	0.024	0.025	0.017	Balance

2.2. Gleeble tests for the annealing investigation

The Gleeble system (model 3180) was used for the preliminary investigation of the local annealing treatment of the dog-bone specimens , whose geometry was designed according to the international standards (ISO 6892). A detailed view of the Gleeble test chamber is shown in Figure 1 : the specimen is gripped by copper grips (which allow the best electric conductivity) and the whole assembly, kept in position by means of a steel frame,

is inserted in the Gleeble clamping system, inside the test chamber. The specimen is heated by Joule effect and the current flow is modulated by a closed loop controller able to minimise the difference between the target temperature and the one acquired by the K-type piloting thermocouple, spot welded on the specimen and indicated as $TC2$ in Figure 1 (tolerance on the test temperature of 2°C).

The heat treatment was characterised by: (i) an initial heating step having a temperature rate approximately equal to 900°C/s, (ii) a soaking phase during which the test temperature (i.e. the one monitored by the piloting thermocouple) was kept constant and (iii) a rapid cooling down to room temperature (air blowing on the sample).

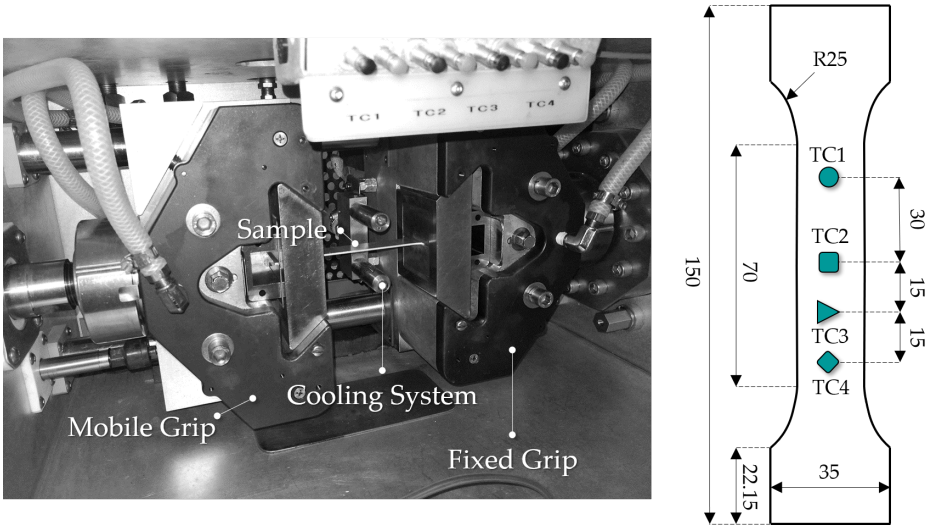

Figure 1: Gleeble 3180 test chamber with the detailed positioning of the 4 thermocouples.

Since the specimen is clamped by cooled jaws, the temperature decreases moving from the centre towards the jaws; the temperature along the specimen was thus approximated by a parabolic distribution at any instant of the

heating test; therefore, the same specimen was simultaneously subjected to different temperature profiles (i.e. heat treatments) according to the position. In order to experimentally define the above mentioned parabolic distribution, the temperature profiles in four points were acquired using 4 thermocouples , as illustrated in Figure 1 . The position of the thermocouples was perfectly known , thus allowing to accurately relate the temperature to each point along the specimen. After the Gleeble test, hardness measurements were conducted along the longitudinal direction (the distance between two consecutive measurements was set to 1 mm). The fully automatic Qness Q10+ hardness tester (load: 0.2 kg; dwell time: 5 s) was used for collecting hardness data along the specimen's longitudinal symmetry path. Thanks to this approach, each hardness value could be univocally related with the correspondent (local) temperature profile.

2.3. Laser heat treatment

Laser heat treatments were conducted using the set up shown in Figure 2. A CO_2 laser source (maximum power: 2500 W) was used. Since the adopted laser head was equipped with a Diffractive Optical Element , the Gaussian energy profile was changed into a squared top-hat one (size: 400 mm^2) which was positioned at the centre of the tensile specimen. In order to improve the absorption , a graphite layer was sprayed on the specimen before the heat treatment (enlargement of Figure 2).

Since samples were heated only in the central area and simultaneously cooled at the two ends, the material experienced a thermal gradient along the longitudinal direction. The laser power and the dwell time were defined according to numerical simulations , which were tuned using data from pre-

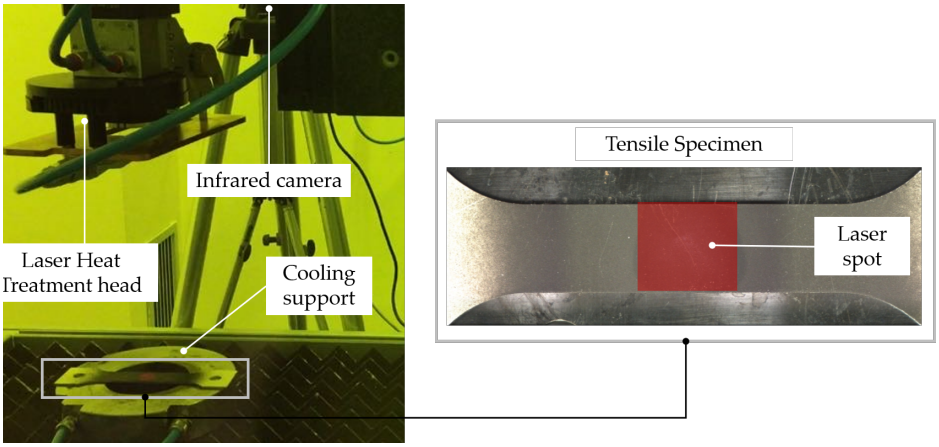

Figure 2: Experimental set up adopted for the Laser Heat treatments and geometry of the specimen.

liminary tests monitored by an infrared camera (FLIR® x6540sc), as better detailed in Section 2.4. Vickers microhardness measurements were performed after the laser heat treatments to evaluate the local change of material properties.

2.4. Numerical model for the laser heat treatment simulation

In order to design the laser annealing, a thermal simulation of the experimental setup described in Section 2.3 was created using the commercial software Abaqus®/Standard: the dog-bone specimen was modelled as a 3D body and meshed with 8-node solid-thermal elements (DC3D8) , characterised by an average dimension of 1 mm. The thermal properties were assumed according to the literature [49]. The heat exchange between the specimen and the surrounding environment, as well as the one between the specimen and the cooling support, was simulated by setting two different values of the Heat Transfer Coefficient (HTC), k_{air} and k_{cooler}, respectively.

The effective fraction of the laser beam energy absorbed by the material was taken into account through the adoption of an absorption coefficient, η. The simulation time was set to 25 s since both the laser heating phase (duration 5.5 s) and the subsequent air cooling phase (duration 19.5 s) were simulated.

The parameters k_{air}, k_{cooler} and η were calibrated through an inverse analysis approach, using data measured from the infrared camera during the above mentioned preliminary laser heating tests , which were performed setting the laser power to 500 W and the dwell time to 5.5 s. An automatic optimization loop, managed by a multi-objective genetic algorithm [50], was created using the commercial software modeFRONTIER® . The automatic procedure could iteratively change the parameters k_{air}, k_{cooler} and η and calculate the difference, in some points of interest, between the temperature predicted by the FE model and the one acquired by the infrared camera. The adopted values of the parameters were the ones able to minimize the above mentioned difference between the numerical and the experimental temperature. The basic principle of the optimization procedure is schematically depicted in Figure 3.

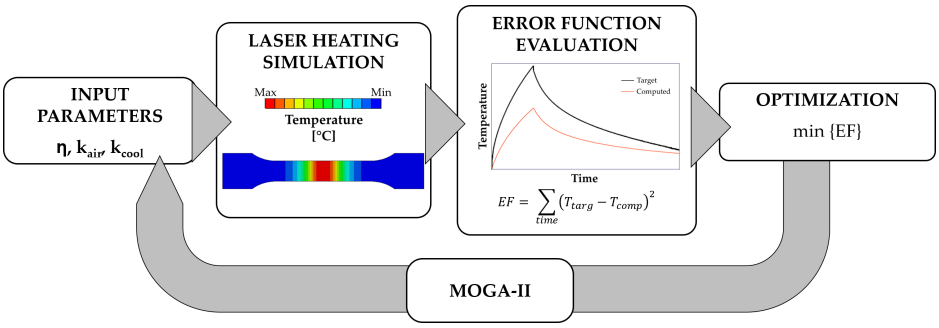

Figure 3: Schematic description of the optimization workflow.

The genetic algorithm started from an initial population consisting of 50 designs (i.e. numerical runs) and evolved through 20 successive generations , thus investigating a totality of 1000 designs in which the value of the parameters was varied within the ranges listed in Table 2. In the same table also the values of the step adopted by the automatic procedure for changing each parameter have been listed

Table 2: List of input variables and the correspondent variation ranges and step.

Input Variable	Lower Bound (LB)	Upper Bound (UB)	Step
η	0	1	0.01
k_{air} $[W/m^2K]$	0	30	0.1
k_{cool} $[W/m^2K]$	0	700	1

Thanks to the inversely calibrated parameters, the FE model could successfully and accurately reproduce the temperature values of the specimen , which were monitored during the heating treatment and acquired at different instants. The accuracy of such an approach will be discussed in Section 3.2.

2.5. Tensile tests on laser heat treated specimens

Tensile tests were performed on laser-heat-treated specimens using an electro-mechanical testing machine (Zwick–Roell® Z050, load cell 50 kN, as depicted in Figure 4) , under quasi-static conditions ($\dot{\varepsilon} = 10^{-4}$ s^{-1}). The correlation between the images observing the specimen deformation history was achieved by means of the commercial software *MatchID*® (`www.matchid.eu`, version 2020.1.1). The details of the 2D-DIC setup and of the adopted correlation settings are listed in Table 3.

Table 3: DIC settings used for tensile tests on uniaxial specimens.

Camera	Pixelink® BU371F
Image resolution	1280×1024, 8-bit
Lens	25 mm C-mount
Polariser	Linear
Field of view	71.92×20 mm
Pixel to mm conversion	1 pixel = 0.08 mm
Patterning Technique	Matt white spray paint base coat with black speckles
Pattern feature size (approx.)	4.2 pixels / 0.3360 mm
DIC technique	2D correlation
DIC software	MatchID®, version 2020.1.1
Image Filtering	Gaussian, 5×5 pixels kernel
Subset size	21 pixels / 1.68 mm
Step size	5 pixels / 0.4 mm
Subset shape function	Affine
Matching criterion	Zero-normalised sum of square differences (ZNSSD)
Interpolant	Bi-cubic spline
Strain formulation	Hencky logarithmic strain
Strain computation	Least-squares differentiation by the convolution method
Spatial smoothing	Savitzky-Golay algorithm, 9×9 window
Temporal smoothing	N/A
Virtual Strain Gauge Size	61 pixels / 4.88 mm
Logarithmic strain noise floor	2.37×10^{-5}

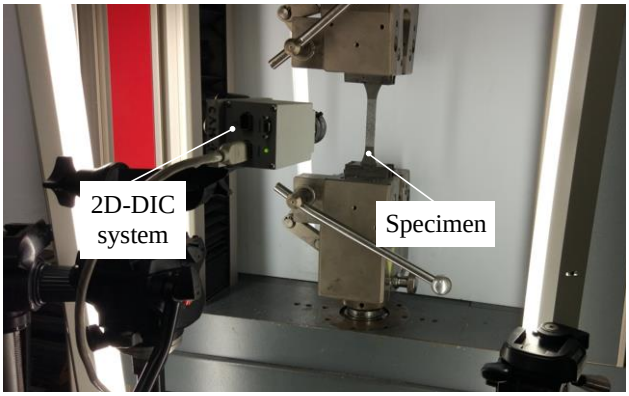

Figure 4: Uniaxial test experimental setup with 2D-DIC system.

3. Results

3.1. Results from annealing tests in the Gleeble system

The heat treatments using the Gleeble system were aimed at evaluating the effects on the material of a very local annealing (i.e. by laser) in a laboratory environment . Gleeble tests were conducted setting the temperature at the piloting thermocouple to 450°C and the soaking time to 10 s. The resulting temperature distribution ranged from 450°C (in the center, where the piloting thermocouple was positioned) to 250°C (close to the Gleeble clamping system); as discussed in Section 2.2, the temperature distribution along the specimen's longitudinal symmetry path was obtained fitting the data acquired by the 4 thermocouples by means of a parabola.

Figure 5a shows the temperature vs. time curves at five different points along the specimen ; such points were selected in order to have the maximum temperature levels changing with a step of 50°C. In the considered points also the Vickers hardness was measured after the Gleeble test . The resulting hardness profile is shown in Figure 5b as a function of the heating

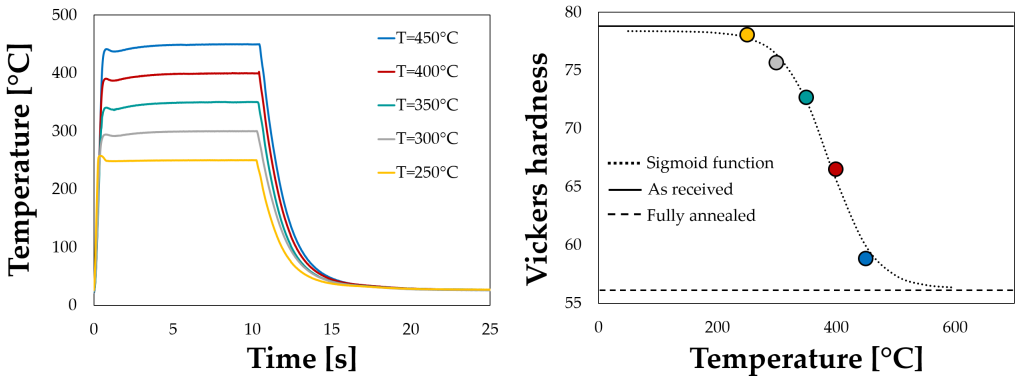

(a) (b)

Figure 5: Results from annealing tests: (a) local temperature-time curves and (b) measured hardness distribution as a function of the peak temperature (i.e. at the soaking step).

temperature (i.e. the maximum temperature T_{peak} experienced by the sample) together with the hardness value of the un-treated material (as-received condition, H32) and of the alloy in the fully annealed condition (H111).

It is worth noticing that, even if the heating rate was very high and the cooling step fast, the treatment cannot be considered "impulsive" and, in particular, the contribution of the cooling phase to the thermal history experienced by the material cannot be neglected. For this reason, an equivalent time (t_{eq}) was adopted, which is defined as the integral bounded by each curve divided by the peak temperature (i.e. the temperature at the soaking step). Each temperature evolution could be thus related to an equivalent time of the corresponding isothermal temperature profile. The average value of the equivalent time , concerning the temperature histories experienced by the material at the 5 monitored points, is equal to 12.68 s.

The following macroscopic variable Ann could be thus defined, which allowed to take into account the level of annealing determined in a certain point by the temperature and the soaking time:

$$Ann = \frac{HV_{ar} - HV_{meas}}{HV_{ar} - HV_{min}}, \tag{1}$$

where the hardness measured along the sample is indicated as HV_{meas}, whereas the maximum (wrought condition) and the minimum hardness (fully annealed condition) are indicated by HV_{ar} and HV_{min}, respectively.

The value of Ann was expressed as a function of the peak temperature T_{peak} using a logistic function (as often made in many engineering and empirical problems [51, 52]):

$$Ann = \frac{1}{1 + exp[-\lambda \cdot (T^* - T_{peak})]}, \tag{2}$$

where the two constants λ and T^* represent the steepness and the midpoint of the sigmoid function, respectively . Such constants were tuned using the experimental results. As shown in Figure 5b, the hardness profile predicted by Eq. 2 (black dotted line) fits very well the experimental values.

3.2. Numerical simulation of the laser heat treatment

At the end of the calibration procedure described in Section 2.4, the following parameters allowed to minimise the discrepancy between numerical and experimental temperature in the 5 points of interest: $\eta = 0.56$, $k_{air} = 23.5\ W/m^2 \cdot K$ and $k_{cooler} = 520\ W/m^2 \cdot K$.

In Figure 6a both the numerical and the experimental temperature profiles at the centre of the specimen's surface which was irradiated by the laser

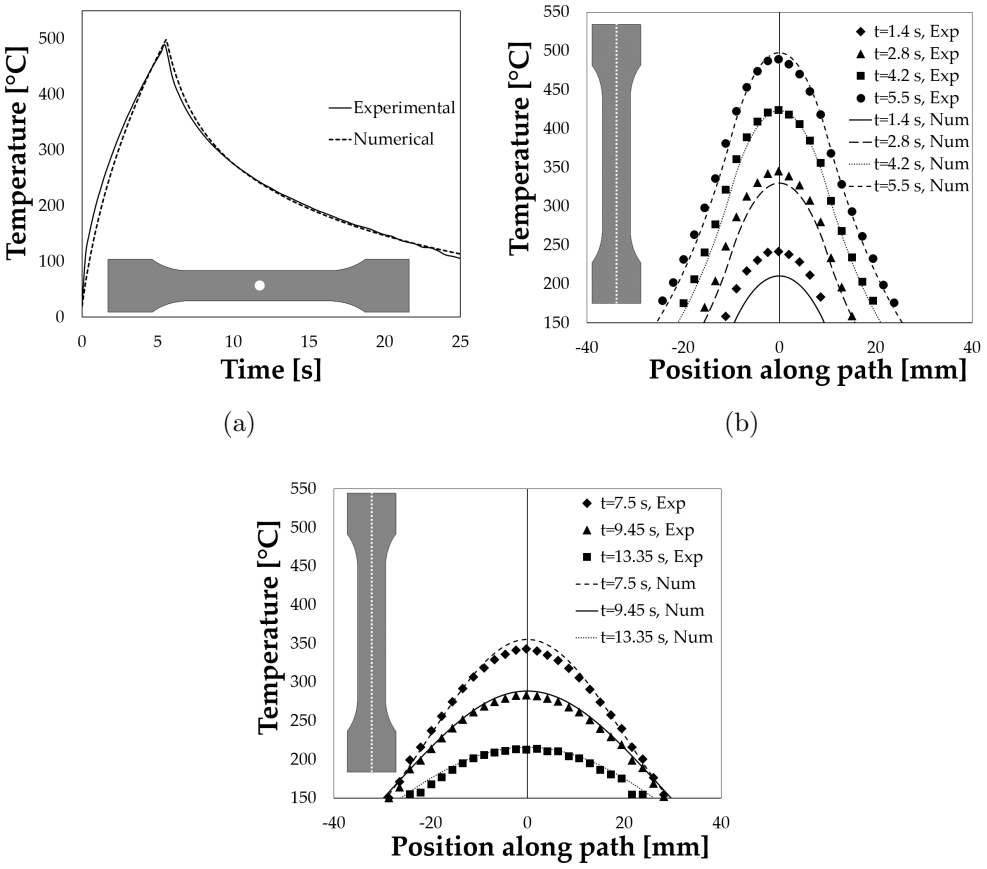

Figure 6: Results from the inverse analysis (experimental data were obtained from the test conducted setting the laser power to 500 W and the dwell time to 5.5 s): a) temperature evolution of the point located at the center of the irradiated surface; temperature distribution during the b) heating and c) cooling down to room temperature.

are plotted . It is worth noticing that the calibrated model was able to accurately reproduce the temperature evolution according to time and position. In addition, the FE model revealed to properly simulate the temperature distribution at different instants of time during both the heating phase (Figure 6b) and the cooling one (Figure 6c).

The inversely tuned model could be thus used to simulate the laser annealing tests on the dog-bone specimens which were then subjected to tensile tests. For such heat treatments, the laser power was set to 750 W and the dwell time to 4 s . Such process conditions resulted to be able to determine the annealing conditions (i.e. temperature levels and, most of all, equivalent time) similar to the ones experienced by the material in the Gleeble tests.

The time-temperature curves obtained by the numerical simulation are shown in Figure 7; in particular, the attention has been focused on the following points of interests along the sample : center, point C; quarter of the laser spot, point Q; border of the laser spot, point E; 3 mm far from point E (approximately within the transition region), point T; far from the heat-affected zone, point B.

It is worth noticing that, even if the heating rate was very high and the cooling step fast, the temperature histor ies were different; however, following the approach described in 3.1, each of them can be considered equivalent to an isothermal one characterized by the peak temperature (T_{peak}) acting on the material for a duration equal to the equivalent time (t_{eq}) . In Table 4 the values of the peak temperature, the equivalent time and the integral below each temperature-time curve are reported for the five points of interest .

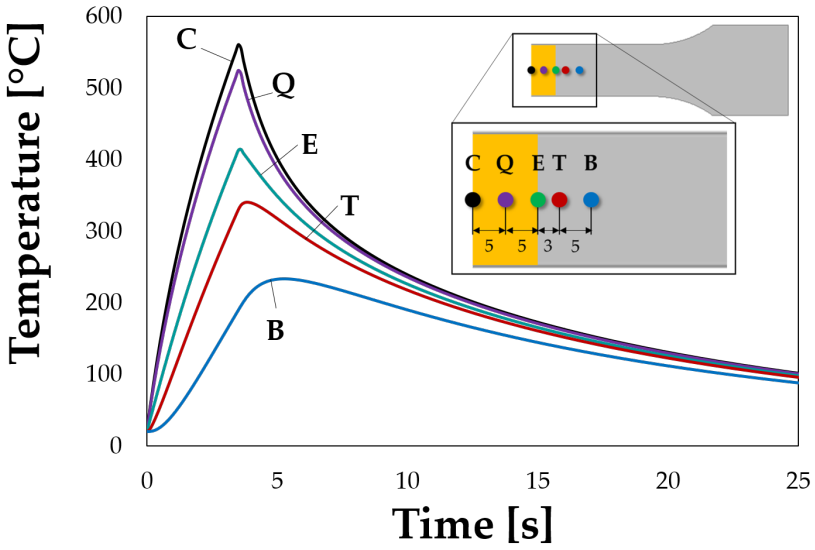

Figure 7: Temperature evolution from the laser heating simulation (laser power: 750 W, dwell time 4s).

The mean equivalent time, calculated as the average of the values at the investigated points of interest, results equal to 12.44 s, which is very close to the value mentioned in 3.1, i.e. 12.68 s, thus Eq. 2 can be reasonably used to analytically predict the hardness distribution of the case study.

Table 4: Integral and equivalent time values of the investigated nodes.

	C	Q	E	T	B
$T_{peak}\ [°C]$	560.89	524.84	414.75	340.29	233.90
$Integral\ [°C \cdot s]$	$5.74 \cdot 10^3$	$5.57 \cdot 10^3$	$5.02 \cdot 10^3$	$4.59 \cdot 10^3$	$3.69 \cdot 10^3$
$t_{eq}\ [s]$	10.24	10.60	12.11	13.50	15.77

3.3. Validation of the annealing function

In order to validate the effectiveness of the proposed approach in determining the level of the annealing through Eq. 2 using the inversely calibrated numerical model, the laser treatment simulated in Section 3.2 (laser power: 750 W; dwell time: 4 s) was experimentally performed. Also in this case the Vickers microhardness was measured along the longitudinal path of the sample . In Figure 8a the whole profile is plotted (position 0 corresponds to the center of the specimen), highlighting the region irradiated by the laser beam (the light yellow box).

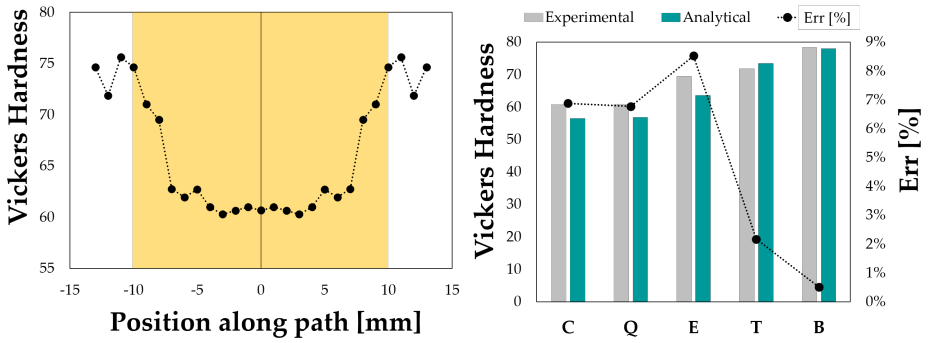

(a) (b)

Figure 8: Local laser heating: a) hardness measurements along the longitudinal path; b) comparison with the predicted values.

It is worth noticing that the laser heating was effective in achieving a sensible drop of the hardness from the initial value of 75.6 HV to 60.3 HV; moreover, the proposed approach resulted to be accurate since, as shown in the bar graph of Figure 8b, it allowed to obtain a satisfactory correspondence between the measured hardness values and the ones predicted using the annealing function . The percentage error was calculated using Eq. 3.

$$Err[\%] = \frac{HV_{exp} - HV_{comp}}{HV_{comp}} * 100\,, \tag{3}$$

where HV_{exp} and HV_{comp} are the experimental and the predicted hardness value; the percentage error, as shown by the dotted black line in Figure 8b, resulted always lower than 9%

3.4. Analysis of the hardening behaviour

So far, the localized heat treatment was evaluated only in terms of hardness. In this section, a deeper investigation was dedicated to the evaluation of the local hardening behaviour in terms of stress vs. strain curves. The laser treated samples were , thus, subjected to the tensile tests assisted by the DIC system.

Figure 9a illustrates the experimental outcomes in terms of strain maps measured at the three different time steps during the tensile test (A, B and C). In addition, the acquired force vs. displacement curve is plotted in Figure 9b. From the very beginning, the full-field measurement revealed distinct material behaviours : in fact, the heat-treated zone experienced a higher strain level under the same loading force compared to the outlying ones, due to the local annealing. At the end of the test, the strain localized at the centre of the specimen, reaching the fracture under a strain level larger than 30%. The maximum strain reached in the zone not affected by the laser treatment was around 5%.

The DIC measurement also allowed to observe a typical feature of the AA5754 , i.e. the random generation of Portevin–Le Chatelier (PLC) bands, which are responsible of the fluctuati on of the force vs. displacement curve

in Figure 9b [53, 54]. However this effect is not relevant in this study and it will not be further commented.

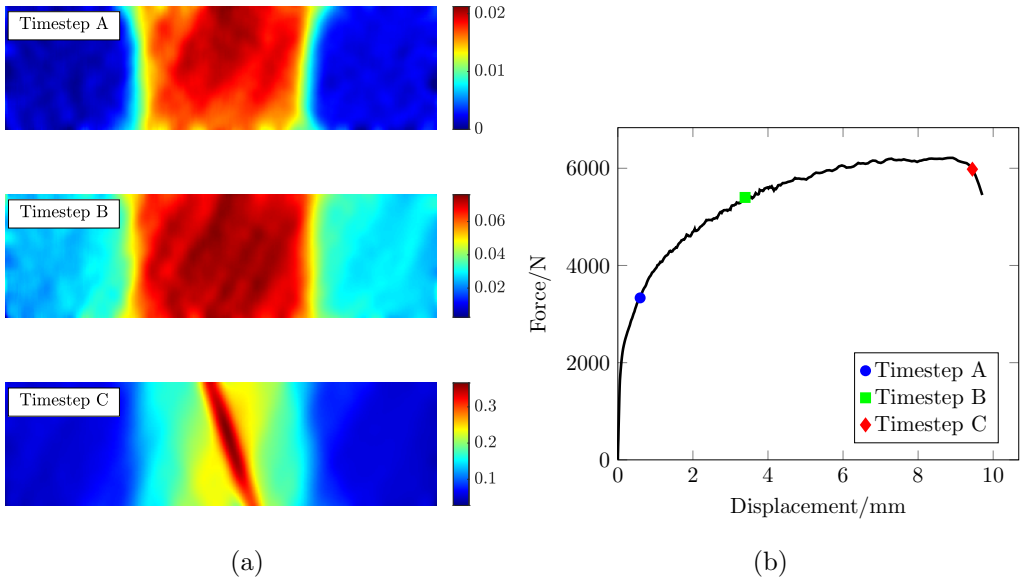

(a) (b)

Figure 9: Uniaxial tensile test experiments on THTB specimens: a) full-field logarithmic ε_{xx} strain component for three timesteps; b) measured total force–displacement curve.

The spatial distribution of the hardening properties was investigated following an approach similar to the subdivision method proposed in [55]. Basically, the whole DIC measurement area was discretized into smaller regions of interest (ROIs), i.e. 31 equally distributed ROIs , characterised by a length of $l = 2.32$ mm . As shown in Figure 10, which refers to the timestep B of Figure 9a, the heat treated zone is clearly detectable from the strain map and its length is approximately equal to $L_{HT} = 26.5$ mm.

Making the assumption of a constant uniaxial stress within each ROI (uniform strain, not changing in the transversal direction), the corresponding stress vs. strain curve could be retrieved. Since the boundary conditions

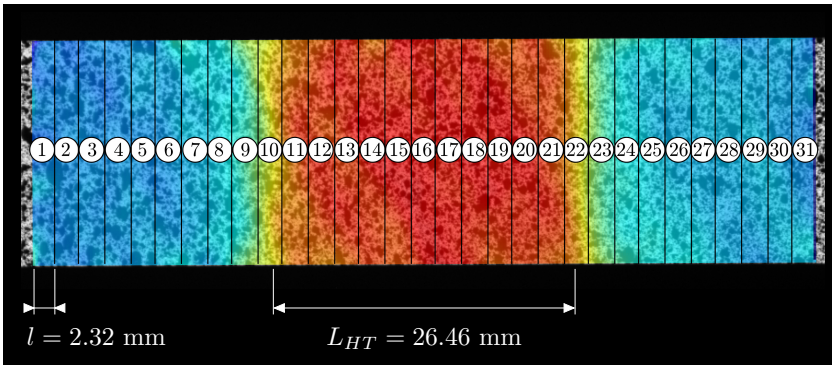

Figure 10: Discretization of the DIC measurement region into smaller ROIs overlapping the strain map at Timestep B.

generated by the uniaxial test made the loading force constant through the gauge length, it was possible to determine the stress and strain curve in each ROI by using the standard true stress relationship $\sigma = \frac{F}{A_0}\exp(\varepsilon)$, where F is the load, A_0 is the initial cross-section area of the specimen and ε indicates the logarithmic strain [56] , which was obtained by averaging the logarithmic strain values derived by the DIC measured displacements in each investigated region . Thereby, a single value for every step of the test could be obtained. The resulting stress vs. strain curves are reported in Figure 11. For the sake of clarity, ROIs having similar behaviour are grouped by color: the blue curves indicate the stress vs. strain relationship from ROIs clearly belonging to the material in the as-received condition; the light blue and orange lines depict the material behaviour in the transition zone; finally, the red color marks the stress vs. strain curves from ROIs in the laser treated zone. This visualization also helps to distinguish the effects of the laser treatment on the material hardening, and to understand its influence on the deformation history of the whole specimen.

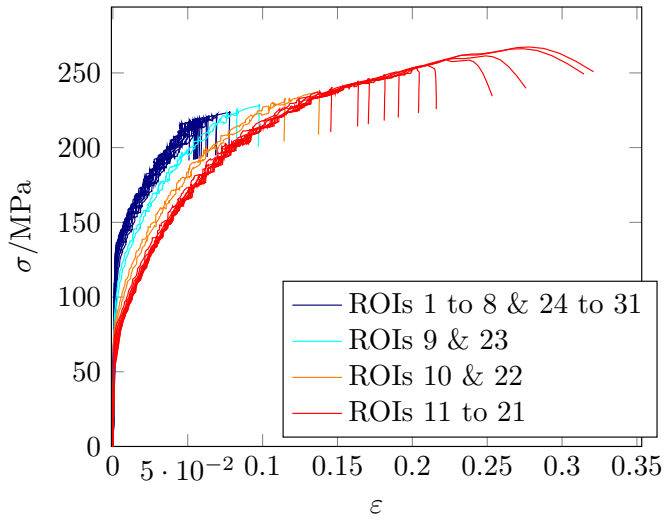

Figure 11: Measured logarithmic stress vs. strain curves from all the ROIs considered. For better understanding the figure, the reader is referred to the web version of the paper.

As expected, the annealing allowed to decrease the initial yield stress, which changed from 135 MPa to about 54 MPa. Afterwards, in the laser treated zone, which experienced the largest plastic deformation, both the necking and the fracture occurred. However, interestingly, the plastic deformation was not only confined in the laser treated zone, but even the un-treated and the transition zones underwent not negligible plastic strain, making thus possible to characterize the hardening behaviour after the yielding. Under the same loading force, ROIs belonging to the annealed part of the specimen reached higher tensile strains, experiencing a higher cross-section reduction compared to the H32 graded ROIs and leading, in turn, to higher stress values.

It is also important to underline that, since the uniaxial assumption is valid only before the occurrence of the diffuse necking, the stress vs. strain

curves beyond this point were not considered in the analysis. The necking point in each flow stress curve was roughly identified by the sudden vertical drops observed in Figure 11.

4. Discussion

4.1. Identification of hardening properties according to the annealing level

The experimental results obtained by the tensile test were used to develop a constitutive model capable of reproducing, at macroscopic level, the effects of the laser treatment in terms of mechanical properties alteration. This is very important to enhance the accuracy of the forming processes simulation through an FE analysis, and the main aim of the present work is to provide a robust methodology for the development of a material model capable of accurately describing the material properties (in terms of flow stress curves) resulting from the very local heat treatment.

Making the assumption that the temperature is almost homogeneous within each ROI of Figure 10, each corresponding stress vs. strain curve in Figure 11 was associated to the temperature T_{peak} (namely the maximum temperature during the heat treatment obtained from the numerical analysis described in Section 2.4). Manipulating the stress vs. strain data, it was possible to show the effect of the annealing at different levels of the strain hardening, identified by the amount of plastic strain ε_p. The results are depicted in Figure 12, which shows the dependency of the flow stress from the peak temperature of the heat treatment considering nine levels of the plastic strain. The stress values were normalized with respect to the stress corresponding to the maximum peak temperature, obtained in ROI 16.

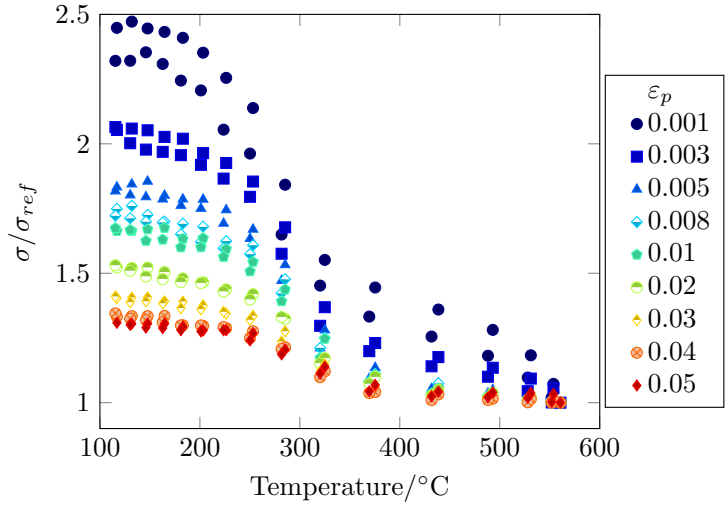

Figure 12: Distribution of the normalised flow stress at different plastic strains, according to the maximum temperature T_{peak} of the heat treatment.

This chart reveals that the effect of the heat treatment changes according to the accumulated plastic strain. For instance, at the early yielding, when $\varepsilon_p = 0.1\%$, the flow stress in the un-treated zone – which experienced a low temperature during the laser treatment – was almost 2.5 times higher than the one in the heat treated zone (reference ROI 16). Afterwards, as the plastic strain increased, the flow stress variance asymptotically stabilized to 1.3.

Figure 12 also suggests a possible method for the description of the hardening behaviour related to the annealing level. Basically, the idea is to define a constitutive model capable of properly modifying a reference flow curve through analytical functions, considering the information from the heat treatment simulation. Following a similar approach as in Section 3.1, the trend of the normalized flow stress can be expressed by means of a sigmoidal

function, as:

$$\frac{\sigma}{\sigma_{ref}}(\varepsilon_p, T_{peak}) = 1 + \frac{A(\varepsilon_p)}{1 + \exp\{-B(\varepsilon_p)[T^*(\varepsilon_p) - T_{peak}]\}}\,. \tag{4}$$

where the parameters $A(\varepsilon_p)$, $B(\varepsilon_p)$ and $T^*(\varepsilon_p)$ regulate the shape of the sigmoid but, unlike Eq. 2, they are affected by the equivalent plastic strain ε_p. In particular, the $A(\varepsilon_p)$ defines the amplitude of the sigmoidal curve that, in other words, characterizes the maximum stress variation between the treated and the un-treated zone. Therefore, this parameter could be defined by directly involving the difference between the flow stress in the annealed zone (σ_{ann}) and the one in the un-treated one (σ_{ar}) at the same amount of the plastic strain, viz.:

$$A(\varepsilon_p) = \frac{\sigma_{ar}(\varepsilon_p)}{\sigma_{ann}(\varepsilon_p)} - 1\,. \tag{5}$$

The parameters $B(\varepsilon_p)$ and $T^*(\varepsilon_p)$ control the slope and the position of the midpoint of the sigmoidal function, respectively. As a consequence, they determine the behaviour of the transition zone.

Differently from $A(\varepsilon_p)$, the interpretation of the dependency of $B(\varepsilon_p)$ and $T^*(\varepsilon_p)$ from the plastic strain ε_p is not straightforward. Therefore, for each level of the investigated plastic strain, the parameters B and T^* were independently calibrated by means of a least square fitting. The resulting values are displayed in Figure 13 as a function of the corresponding amount of ε_p. As shown in Figure 13a, the parameter B increases until $\varepsilon_p = 1\%$, then its trend becomes almost constant; therefore, it could be described by using the following function:

$$B(\varepsilon_p) = \beta \tanh \frac{\varepsilon_p}{\varepsilon_0} + c_\beta \,, \tag{6}$$

where, β, c_β and ε_0 are coefficients to be calibrated using experimental data.

On the other hand, Figure 13b shows that the parameter $T^*(\varepsilon_p)$ is characterised by a trend that can be assumed constant, i.e. $T^*(\varepsilon_p) = T^*$.

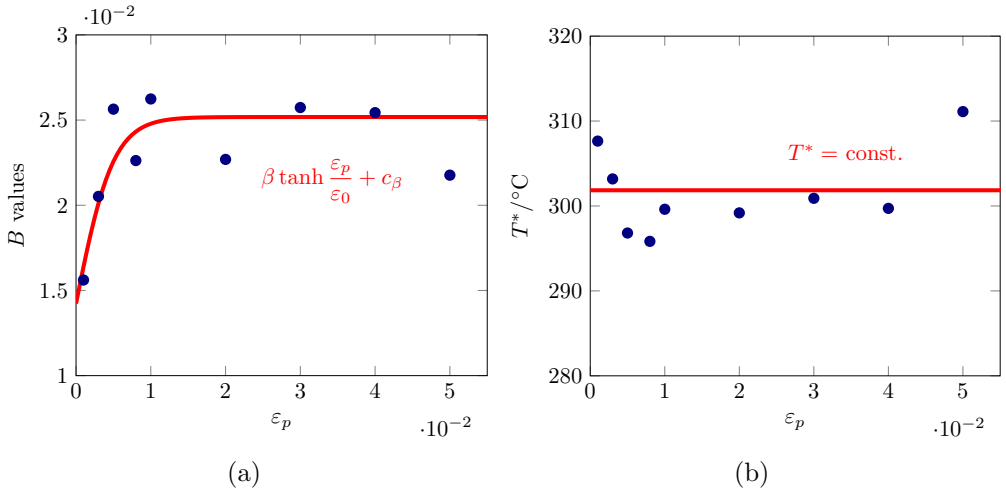

Figure 13: Dependence of sigmoidal function parameters $B(\varepsilon_p)$ and $T^*(\varepsilon_p)$ from plastic strain.

The expressions in Eq. 5 and 6 can be replaced in Eq. 4 and, after few manipulations, it is possible to define a general expression of the hardening behaviour determined by the local heat treatment (in this case identified by the peak temperature T_{peak}) regulated by four coefficients (β, c_β, T^*, ε_0):

$$\sigma(\varepsilon_p, T_{peak}) = \sigma_{ann}(\varepsilon_p) + \frac{\sigma_{ar}(\varepsilon_p) - \sigma_{ann}(\varepsilon_p)}{1 + \exp\left\{ -\left[\beta \, \tanh\left(\frac{\varepsilon_p}{\varepsilon_0} \right) + c_\beta \right] \left(T^* - T_{peak} \right) \right\}} \,, \tag{7}$$

It is worth noting that such a function , which will be referred as HT-hardening model, can be calibrated through a single test, as better detailed in the next section.

4.2. Material model validation

In this section, Eq. 7 is calibrated and used to predict the hardening behavior of AA5754 specimens after the laser treatment.

The calibration was performed in two steps: first the hardening curves σ_{ann} and σ_{ar} were identified and, afterwards, the four coefficients related to the sigmoidal function were evaluated. Dealing with complex constitutive models, a multiple step identification procedure can indeed enhance the computational efficiency and results' accuracy of the identification process, as reported in [43].

The hardening curves σ_{ann} and σ_{ar} were described using a modified Voce law:

$$\sigma(\varepsilon_p) = Y(1 + \varepsilon_p) - Re^{-b\varepsilon_p}\,, \tag{8}$$

where Y, R and b are the material model coefficients (obtained by a least-square matching to the experimental data) and ε_p is the equivalent plastic strain. Specifically, σ_{ann} was calibrated using the experimental stress vs. strain curve from ROI 16, in which the peak temperature experienced by the material was maximum ; on the contrary, σ_{ar} was calibrated using the results from ROI 1, since, in this region, the material is almost unaffected by the annealing (see Figure 10). The identified parameters are listed in Table 5:

Table 5: Modified Voce hardening law coefficients for the two curves σ_{ann} and σ_{ar}.

	Y	R	b
σ_{ann} (ROI 16)	213.26	148.53	20.08
σ_{ar} (ROI 1)	232.74	98.32	26.99

Finally, the four coefficients regulating the sigmoidal function in Eq. 7 were inversely calibrated using data from all ROIs. In order to minimize the error between the experimental and the predicted flow curves , the SQP algorithm (Matlab® *fmincon* function) was used . The resulting coefficients are listed in Table 6.

Table 6: Identified coefficients for the HT-hardening model.

β	c_β	$T^*/°C$	ε_0
0.01095	0.01423	301.85	0.005

Figure 14 illustrates the outcomes of the identification procedure. In particular, Figure 14a shows the comparison between the experimental curves obtained in five different ROIs and the corresponding curves predicted by the calibrated model: a good agreement can be seen in all cases.

A further comparison is presented in Figure 14b, where the effect of the local annealing is illustrated in terms of the normalized flow stress for different levels of the equivalent plastic strain (similar to Figure 12). Also in this case the proposed model reveals to be able to correctly reproduce the experimental results, although a small mismatch is visible for the lowest value of the equivalent plastic strain (when T_{peak} is in the range of 350-550 °C).

However, such a mismatch is expected to have a minor impact on the accuracy of the model – especially for the FE simulations of sheet metal forming operations – since it disappears when ε_p >0.005.

4.3. Implementation of the material model into a numerical simulation.

In order to verify the effectiveness of the proposed approach for modelling the local material behaviour determined by the laser heat treatment, the HT-hardening model was implemented into a FE simulation of the tensile test detailed in 3.4. Such a conclusive step plays a fundamental role to establish a complete simulation tool for the analysis and the design of sheet metal forming operations at room temperature.

Therefore, the material model evaluated using the proposed methodology was introduced into the Abaqus/Standard® solver through an user material subroutine (UMAT) , aimed at effectively simulating the gradient of material properties determined by the laser treatment.

In this work, an isotropic plastic behaviour was used, but the same approach is readily extendable to the anisotropic plasticity. The stress reconstruction from the strain data was carried out following the implicit algorithm in [57], which already proved its robustness especially when used with non-quadratic anisotropic yielding functions [58]. In addition, since the complete numerical investigation of the problem required the annealing information from the laser heat treatment, the structural analysis was linked to the transient thermal analysis. The framework of whole simulation process, summarized in Figure 15, is organized as follows:

- *Local heat treatment simulation*: a 3D transient thermal analysis is used to simulate the local heat treatment according to the preliminary

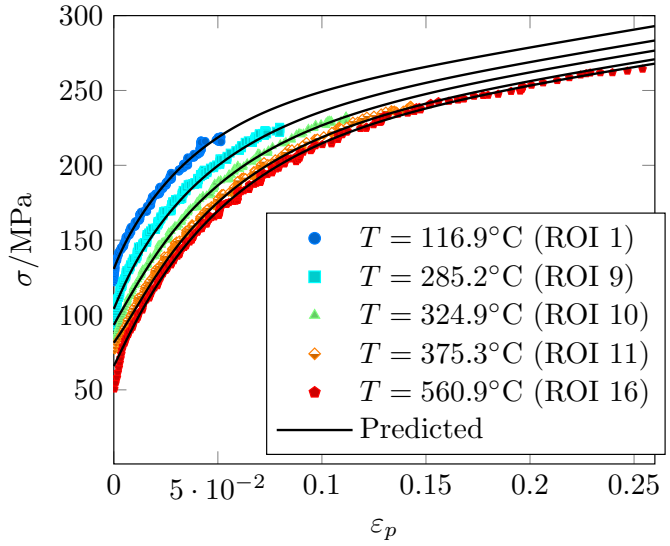

(a)

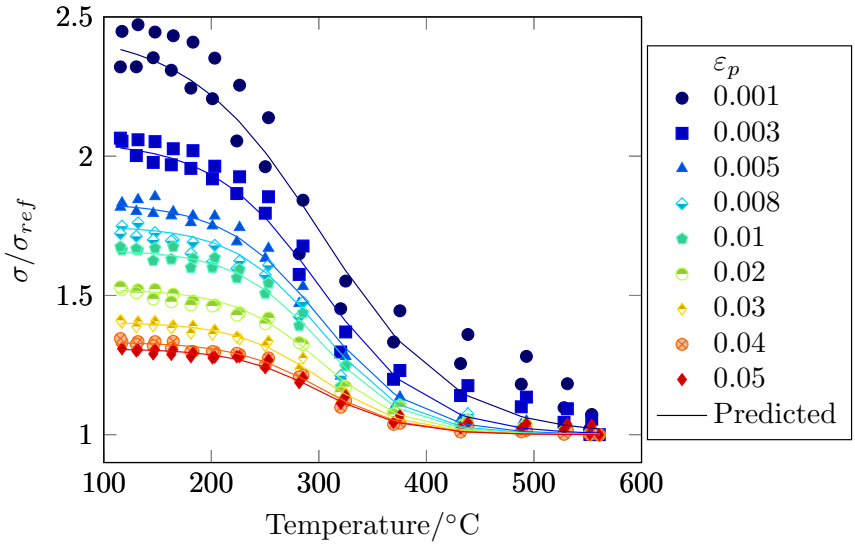

(b)

Figure 14: Predicted hardening behaviour with the calibrated model a) comparison with experimental flow curves for 5 different ROIs, b) comparison in terms of normalized stress at different levels of the plastic strain.

information given by the annealing function, being the aim to obtain the temperature distribution along the specimen and the temperature profile at each node.

- *Interpolation of* T_{peak}: the maximum temperature T_{peak} at each node is exported to the structural model used for the simulation of the sheet metal forming operation at room temperature.

- *Structural analysis*: the non-linear analysis of the sheet metal forming process is performed and the HT-hardening model is implemented (through the UMAT) to locally define the material properties (as a function of T_{peak}).

The specimen was discretized into 2700 4-node fully-integration quadrilateral elements (0.7×0.7 mm^2); the boundary conditions of the tensile test were numerically reproduced by pinning all the nodes on the left end of the specimen and by controlling the displacement of the right side according to the measured loading history.

A second model was developed using the more common approach in which the specimen is partitioned into different zones; in the investigated case study, the sample was divided into three zones and two different material properties were assigned: the fully annealed material behaviour, i.e. $\sigma_{ann}(\varepsilon_p)$ of Section 4.2, was assigned to the central partition, whose length was set to L_{HT} (see Figure 10), while $\sigma_{ar}(\varepsilon_p)$ was assigned to the two peripheral zones (without any transition of the post–heating properties between the two material conditions).

Figure 16 compares the logarithmic strain maps obtained from the FEM

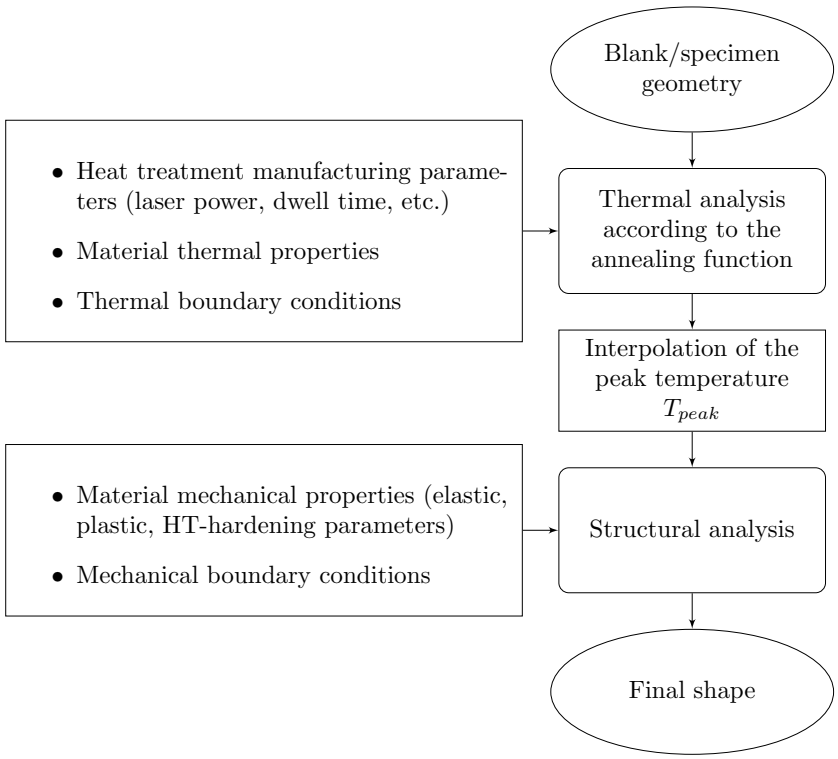

Figure 15: Numerical simulation framework for the THTB manufacturing process and the following sheet metal forming operation.

simulations performed using the above described approaches with the strain field derived the DIC deformation measurement at three different loading steps.

The numerical model implementing the HT-hardening model appears to be capable of accurately capturing the heterogeneous strain field, even when the necking occurs (Figure 16c). On the other side, the simulation strategy based on the qualitative assignment of the material properties throughout the partitioning of the region which is deformed led to a poor description of the strain field. As expected, the abrupt changing of material properties

generated a strain localization in proximity of the border of the heat treated zone and, as a consequence, an imprecise distribution of the generated shear strain. Such a difference become more significant when the stroke increased, thus producing a concave feature in the neighbourhood of the partition line. As shown in Figure 17, the proposed approach even allows to enhance the prediction of the loading force. The HT-hardening model, in fact, appears to be able to reproduce the experimental force vs. displacement curve, reducing the 5% gap observed when the qualitative modelling based on partitions is used.

In addition, it is worth underlying that, using the proposed approach, there is no need of partitioning the FE model into different areas but the heterogeneous properties of the blank sheet are automatically and accurately set according to the T_{peak} distribution. Therefore, this approach is likely to simplify and improve the forming simulations of blanks with complex localized heat treated patterns for industrial applications, where partitioning could even become impossible to be performed, especially when multiple heat treatment parameters are considered (not only the temperature but, for example, also the time).

5. Conclusions

The definition of a fast and, at the same time, accurate methodology for the material characterization is a fundamental step for the correct design of manufacturing processes. This is particularly important when a sheet metal forming operation using a material with graded properties , obtained, like in the present work, through an heat treatment performed by laser, has

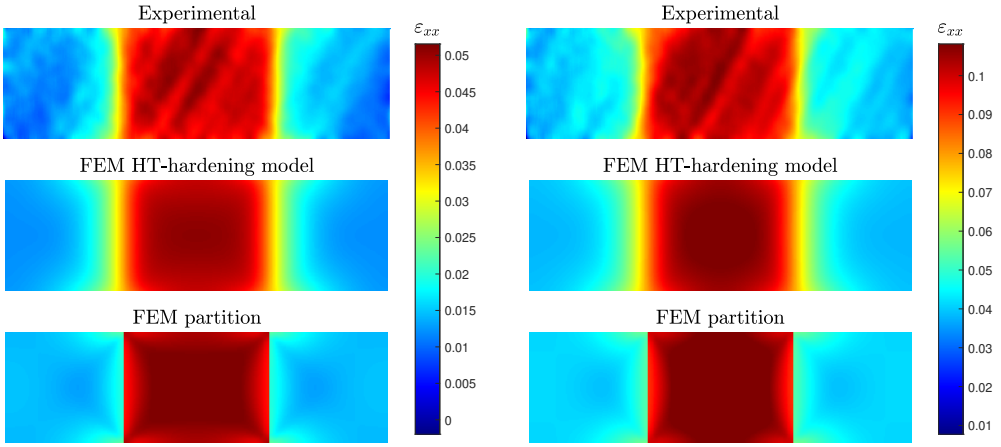

(a) $U_x = 2$ mm.

(b) $U_x = 5$ mm.

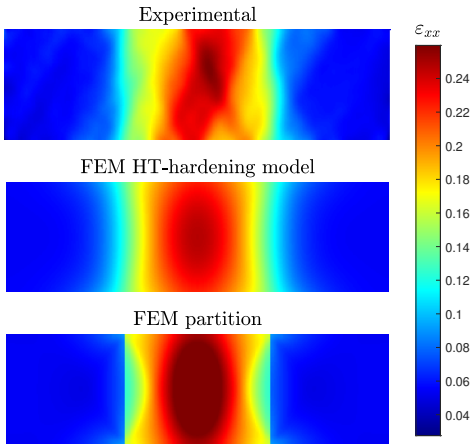

(c) $U_x = 9$ mm.

Figure 16: Comparison between numerical strain fields ε_{xx} and DIC data at three different horizontal displacement loads U_x along the test's time history.

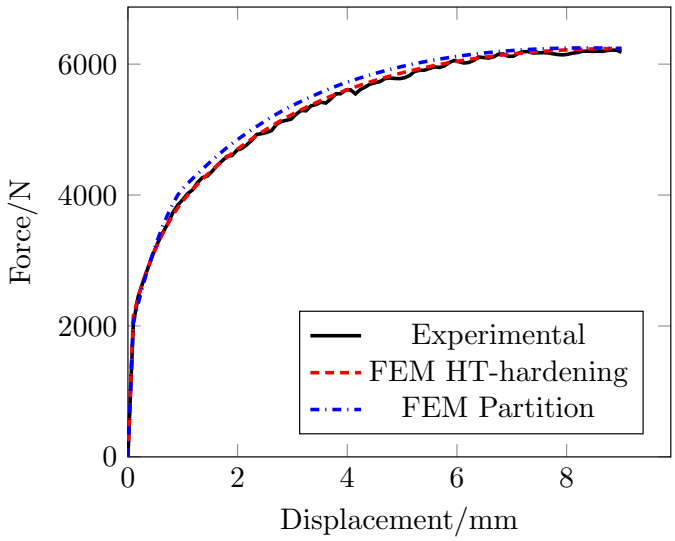

Figure 17: Comparison of force-displacement curves between the two THTB simulation strategies and the experimental data.

to be designed. The methodology proposed by the authors is thus aimed at characterizing the non-linear plastic behavior of a strain-hardenable Al alloy (AA5754) in a wrought condition (H32) but locally brought to a fully or partially annealed state via laser heating.

Data from Vickers microhardness tests after preliminary heat treatments using the Gleeble system allowed to evaluate an annealing function (Ann) ; the post-heating properties could be thus correlated to the local temperature history by means of a sigmoidal function.

The inverse analysis allowed to effectively tune a finite element thermal model able to optimally simulate the laser treatment. Combining the results obtained from an accurate thermal simulation and the information about the material alteration given by the annealing function (Ann), the laser heat treatment could be correctly designed and the change of material

properties in terms of hardness accurately predicted, as confirmed by the good matching between experimental and numerical data.

The possibility to assess the hardening behaviour (flow stress curves) by means of a unique tensile test assisted by the DIC system was also demonstrated: the monitored area was subdivided in regions of interest, so that the local evolution of the stress state could be calculated and related to the same temperature parameter (T_{peak}) used for defining the annealing function. In fact, using again a sigmoidal function, the flow stress behaviour could be implemented in the numerical simulation of the tensile test ; the obtained results revealed to be in a very good agreement with the experimental data, thus demonstrating the effectiveness of the adopted methodology.

It becomes clear that the proposed approach is capable of providing a comprehensive understanding of several material conditions drastically reducing the number of test to be performed (a single test suffices), thus making the characterization methodology less time and material consuming. Moreover, the strict correlation between the stress state and the variables related to the heating step (in the specific case, the maximum temperature reached during the laser heating, T_{peak}) makes the proposed hardening model general and versatile, thus being applicable to any Al alloys or even to any material in wrought condition.

The adoption of an FE-based approach was intentionally pursued by the authors to emphasize the importance of having a robust and accurate numerical tool. In fact, in order to successfully and effectively modify the local behavior of a material aiming at improving its stamping attitude, it is necessary to properly design the laser treatment. For such a goal the FE

simulation is crucial, since it allows: (i) to design the heat treatment for any industrial part (different from the benchmark one investigated in the present work) without acquiring any temperature map and (ii) to investigate different strategies without any time and cost consuming experimental test. Thereby, the simulation of any subsequent forming process is feasible and accurate: in fact, thanks to the local assignment of the material properties according to the local heating conditions (evaluated by means of the specific annealing function), the quality of the numerical predictions can be remarkably improved.

Acknowledgements

The present paper received funding from the Italian Ministry of Economic Development, MISE (Project "FORTRAIN").

References

[1] Caneon Kurien, Ajay Kumar Srivastava, and Emeric Molere. Emission control strategies for automotive engines with scope for deployment of solar based e-vehicle charging infrastructure. *Environmental Progress & Sustainable Energy*, page e13267, 2019.

[2] Alan Taub, Emmanuel De Moor, Alan Luo, David K. Matlock, John G. Speer, and Uday Vaidya. Materials for automotive lightweighting. *Annual Review of Materials Research*, 49(1):327–359, 2019.

[3] A. Vadiraj, M. Abraham, and A.S. Bharadwaj. *Trends in Automotive Light Weighting*, pages 89–102. Springer, 2019".

[4] Anne Marie Lewis, Jarod C Kelly, and Gregory A Keoleian. Vehicle lightweighting vs. electrification: life cycle energy and ghg emissions results for diverse powertrain vehicles. *Applied Energy*, 126:13–20, 2014.

[5] Juan C González Palencia, Takaaki Furubayashi, and Toshihiko Nakata. Energy use and co2 emissions reduction potential in passenger car fleet using zero emission vehicles and lightweight materials. *Energy*, 48(1):548–565, 2012.

[6] Hyung-Ju Kim, Gregory A Keoleian, and Steven J Skerlos. Economic assessment of greenhouse gas emissions reduction by vehicle lightweighting using aluminum and high-strength steel. *Journal of Industrial Ecology*, 15(1):64–80, 2011.

[7] G Meschut, V Janzen, and T Olfermann. Innovative and highly productive joining technologies for multi-material lightweight car body structures. *Journal of Materials Engineering and Performance*, 23(5):1515–1523, 2014.

[8] W.S. Miller, L. Zhuang, J. Bottema, A.J. Wittebrood, P. De Smet, A. Haszler, and A. Vieregge. Recent development in aluminium alloys for the automotive industry. *JMaterials Science and Engineering A*, 280:37–49, 2000.

[9] R. Kuziak, R. Kawalla, and S. Waengler Advanced high strength steels for automotive industry. *Archives of Civil and Mechanical Engineering*, 8(2), 2008.

[10] Alex Poznak, Daniel Freiberg, and Paul Sanders. Automotive wrought aluminium alloys. In *Fundamentals of Aluminium Metallurgy*, pages 333–386. Elsevier, 2018.

[11] K.K. Dama, V.S. Babu and R.N. Rao. State of the art on automotive lightweight body-in-white design. *Materials Today: Proceedings*, 5(10, Part 1):20966 – 20971, 2018. International Conference on Smart Engineering Materials (ICSEM 2016), October 20-22, 2016.

[12] Jürgen Hirsch. Recent development in aluminium for automotive applications. *Transactions of Nonferrous Metals Society of China*, 24(7):1995–2002, 2014.

[13] S Kalpakjian and SR Schmid. Manufacturing processes for engineering materials–5th edition. *agenda*, 12:1, 2014.

[14] Kailun Zheng, Denis J Politis, Liliang Wang, and Jianguo Lin. A review on forming techniques for manufacturing lightweight complex—shaped aluminium panel components. *International Journal of Lightweight Materials and Manufacture*, 1(2):55–80, 2018.

[15] Serkan Toros, Fahrettin Ozturk, and Ilyas Kacar. Review of warm forming of aluminum–magnesium alloys. *Journal of Materials Processing Technology*, 207(1-3):1–12, 2008.

[16] G Palumbo and L Tricarico. Numerical and experimental investigations on the warm deep drawing process of circular aluminum alloy specimens. *Journal of materials processing technology*, 184(1-3):115–123, 2007.

[17] G Palumbo and A Piccininni. Numerical–experimental investigations on the manufacturing of an aluminium bipolar plate for proton exchange membrane fuel cells by warm hydroforming. *The International Journal of Advanced Manufacturing Technology*, 69(1-4):731–742, 2013.

[18] H Laurent, J Coër, PY Manach, MC Oliveira, and LF Menezes. Experimental and numerical studies on the warm deep drawing of an al–mg alloy. *International Journal of Mechanical Sciences*, 93:59–72, 2015.

[19] Tegan McAnulty, Jack Jeswiet, and Matthew Doolan. Formability in single point incremental forming: A comparative analysis of the state of the art. *CIRP Journal of Manufacturing Science and Technology*, 16:43–54, 2017.

[20] G Palumbo. Hydroforming a small scale aluminum automotive component using a layered die. *Materials & Design*, 44:365–373, 2013.

[21] Antonio Piccininni and Gianfranco Palumbo. Design and optimization of the local laser treatment to improve the formability of age hardenable aluminium alloys. *Materials*, 13(7):1576, 2020.

[22] Manfred Geiger, Marion Merklein, and Uwe Vogt. Aluminum tailored heat treated blanks. *Production Engineering*, 3(4-5):401, 2009.

[23] G Palumbo, SH Zhang, L Tricarico, C Xu, and LX Zhou. Numerical/experimental investigations for enhancing the sheet hydroforming process. *International Journal of Machine Tools and Manufacture*, 46(11):1212–1221, 2006.

[24] G Ambrogio, L Filice, and F Gagliardi. Formability of lightweight alloys by hot incremental sheet forming. *Materials & Design*, 34:501–508, 2012.

[25] G Palumbo, A Piccininni, P Guglielmi, and G Di Michele. Warm hydroforming of the heat treatable aluminium alloy ac170px. *Journal of Manufacturing Processes*, 20:24–32, 2015.

[26] Antonio Piccininni, Gabriella Di Michele, Gianfranco Palumbo, Donato Sorgente, and Luigi Tricarico. Improving the hydromechanical deep-drawing process using aluminum tailored heat treated blanks. *Acta Metallurgica Sinica (English Letters)*, 28(12):1482–1489, 2015.

[27] Alexander Kahrimanidis, Michael Lechner, Julia Degner, Daniel Wortberg, and Marion Merklein. Process design of aluminum tailor heat treated blanks. *Materials*, 8(12):8524–8538, 2015.

[28] V.R. Sagar, K. Wärmefjord and R. Söderberg. Influence of Selective Laser Heat Treatment Pattern Position on Geometrical Variation. *Journal of Manufacturing Science and Engineering*, 141(4), 2019.

[29] Marco Rossi and Fabrice Pierron. On the use of simulated experiments in designing tests for material characterization from full-field measurements. *International Journal of Solids and Structures*, 49(3-4):420–435, 2012.

[30] N Souto, A Andrade-Campos, and S Thuillier. Mechanical design of a heterogeneous test for material parameters identification. *International Journal of Material Forming*, 10(3):353–367, 2017.

[31] Gianfranco Palumbo, Vito Piglionico, Antonio Piccininni, Pasquale Guglielmi, Donato Sorgente, and Luigi Tricarico. Determination of interfacial heat transfer coefficients in a sand mould casting process using an optimised inverse analysis. *Applied Thermal Engineering*, 78:682–694, 2015.

[32] Stéphane Avril, Marc Bonnet, Anne-Sophie Bretelle, Michel Grédiac, François Hild, Patrick Ienny, Félix Latourte, Didier Lemosse, Stéphane Pagano, Emmanuel Pagnacco, et al. Overview of identification methods of mechanical parameters based on full-field measurements. *Experimental Mechanics*, 48(4):381, 2008.

[33] Dario Amodio, Giovanni B Broggiato, Francesca Campana, and Golam M Newaz. Digital speckle correlation for strain measurement by image analysis. *Experimental Mechanics*, 43(4):396–402, 2003.

[34] Michael A Sutton, Jean Jose Orteu, and Hubert Schreier. *Image correlation for shape, motion and deformation measurements: basic concepts, theory and applications*. Springer Science & Business Media, 2009.

[35] Jörgen Kajberg and Göran Lindkvist. Characterisation of materials subjected to large strains by inverse modelling based on in-plane displacement fields. *International Journal of Solids and Structures*, 41(13):3439–3459, 2004.

[36] David Lecompte, Steven Cooreman, Sam Coppieters, John Vantomme, Hugo Sol, and Dimitri Debruyne. Parameter identification for anisotropic plasticity model using digital image correlation: Compari-

son between uni-axial and bi-axial tensile testing. *European Journal of Computational Mechanics/Revue Européenne de Mécanique Numérique*, 18(3-4):393–418, 2009.

[37] Kristof Denys, Sam Coppieters, Marc Seefeldt, and Dimitri Debruyne. Multi-dic setup for the identification of a 3d anisotropic yield surface of thick high strength steel using a double perforated specimen. *Mechanics of Materials*, 100:96–108, 2016.

[38] Fabrice Pierron and Michel Grédiac. *The virtual fields method: extracting constitutive mechanical parameters from full-field deformation measurements*. Springer Science & Business Media, 2012.

[39] Marco Rossi, Fabrice Pierron, and Michaela Štamborská. Application of the virtual fields method to large strain anisotropic plasticity. *International Journal of Solids and Structures*, 97:322–335, 2016.

[40] JMP Martins, A Andrade-Campos, and S Thuillier. Calibration of anisotropic plasticity models using a biaxial test and the virtual fields method. *International Journal of Solids and Structures*, 172:21–37, 2019.

[41] Aleksander Marek, Frances M Davis, and Fabrice Pierron. Sensitivity-based virtual fields for the non-linear virtual fields method. *Computational mechanics*, 60(3):409–431, 2017.

[42] Aleksander Marek, Frances M Davis, Marco Rossi, and Fabrice Pierron. Extension of the sensitivity-based virtual fields to large deformation anisotropic plasticity. *International Journal of Material Forming*, 12(3):457–476, 2019.

[43] A. Lattanzi, F. Barlat, F. Pierron, A. Marek, and M. Rossi. Inverse identification strategies for the characterization of transformation-based anisotropic plasticity models with the non-linear VFM. *International Journal of Mechanical Sciences*, 173:105422, 2020.

[44] L Wang and W Tong. Identification of post-necking strain hardening behavior of thin sheet metals from image-based surface strain data in uniaxial tension tests. *International journal of solids and structures*, 75:12–31, 2015.

[45] Marco Rossi, Attilio Lattanzi, and Frederic Barlat. A general linear method to evaluate the hardening behaviour of metals at large strain with full-field measurements. *Strain*, 54(3):e12265, 2018.

[46] MA Sutton, JH Yan, Stéphane Avril, Fabrice Pierron, and SM Adeeb. Identification of heterogeneous constitutive parameters in a welded specimen: uniform stress and virtual fields methods for material property estimation. *Experimental Mechanics*, 48(4):451–464, 2008.

[47] G Le Louëdec, F Pierron, Michael A Sutton, and Anthony P Reynolds. Identification of the local elasto-plastic behavior of fsw welds using the virtual fields method. *Experimental Mechanics*, 53(5):849–859, 2013.

[48] António Andrade-Campos, Sandrine Thuillier, João Martins, Pierpaolo Carlone, Fausto Tucci, Robertt Valente, Rui MF Paulo, and Ricardo J Alves de Sousa. Integrated design in welding and incremental forming: Material model calibration for friction stir welded blanks. *Procedia Manufacturing*, 47:429–434, 2020.

[49] O. El Fakir, L. Wang, D. Balint, J.P. Dear, J. Lin, and T.A. Dean. Numerical study of the solution heat treatment, forming, and in-die quenching (HFQ) process on AA5754. *International Journal of Machine Tools and Manufacture*, 87:39–48, 2014.

[50] S. Poles, E. Rigoni, and T. Robic. MOGA-II performance on noisy optimization problems. In *International Conference on Bioinspired Optimization Methods and their Applications, Ljubljana, Slovenia*, 2004.

[51] Edward L. Spitznagel. 6 logistic regression. In C.R. Rao, J.P. Miller, and D.C. Rao, editors, *Epidemiology and Medical Statistics*, volume 27 of *Handbook of Statistics*, pages 187 – 209. Elsevier, 2007.

[52] F.J. Richards. A flexible growth function for empirical use. *Journal of Experimental Botany*, 10:290–301, 1959.

[53] J. Kang, D. Wilkinson, M. Jain, J. Embury, A. Beaudoin, S. Kim, R. Mishira, and A. Sachdev. On the sequence of inhomogeneous deformation processes occurring during tensile deformation of strip cast AA5754. *Acta Materialia*, 54:209–218, 2006.

[54] H. Halim, D.S. Wilkinson, and M. Niewczas. The Portevin–Le Chatelier (PLC) effect and shear band formation in an AA5754 alloy. *Acta Materialia*, 55:4151–4160, 2007.

[55] M. Rossi, A. Lattanzi, A. Piccininni, P. Guglielmi, and G. Palumbo. Study of tailor heat treated blanks using the Fourier-series-based VFM. *Procedia Manufactoring*, 47:904–909, 2020.

[56] Albrecht Bertram. *Elasticity and Plasticity of Large Deformations*. Springer, 2008.

[57] J.W. Yoon, D.Y. Yang, K. Chung, and F. Barlat. A general elasto-plastic finite element formulation based on incremental deformation theory for planar anisotropy and its application to sheet metal forming. *International Journal of Plasticity*, 15:35–67, 1999.

[58] J.W. Yoon, F. Barlat, R.E. Dick, K. Chung, and Kang T.J. Plane stress yield function for aluminum alloy sheets — part II: FE formulation and its implementation. *International Journal of Plasticity*, 20:495–522, 2004.